Individual and joint inversion of head and flux data by geostatistical hydraulic tomography

Behzad Pouladi [1*], Niklas Linde[2], Laurent Longuevergne[1], Olivier Bour[1]

[1] Univ Rennes, CNRS, Géosciences Rennes, UMR 6118, 35000 Rennes, France.

[2] University of Lausanne, Institute of Earth Sciences, Lausanne, Switzerland

ABSTRACT

Hydraulic tomography is a state-of-the-art method for inferring hydraulic conductivity fields using head data. We employed geostatistical inversion using synthetically generated head and flux data individually and jointly to better understand the relative merits of each data type. For the typical case of a small number of observation points, we find that flux data provide a better resolved hydraulic conductivity field compared to head data when considering data with similar signal-to-noise ratios. This finding is further confirmed by a resolution analysis. When considering a high number of observation points, the estimated fields are of similar quality regardless of the data type. In terms of borehole boundary conditions, the best setting for flux and head data are constant head and constant rate, respectively, while joint inversion results are insensitive to the borehole boundary type. When considering the same number of observations, the joint inversion of head and flux data does not offer advantages over individual inversions. When considering the same number of observation points and, hence, twice as many observations, the joint inversion performs better than individual inversions. The findings of this paper are useful for future planning and design of hydraulic tomography tests comprising flux and head data.

KEYWORDS: hydraulic tomography, groundwater flux, geostatistical inversion, principal component geostatistical analysis (PCGA), resolution analysis

1. INTRODUCTION

Knowledge of hydraulic conductivity distributions is essential for the management of water resources (Liu et al., 2020), solute transport predictions (Yeh, 1992; Jiménez, 2015) and designing remediation of contaminated sites (Fakhreddine et al., 2016). A variety of geophysical (Kowalsky et al., 2004; Revil et al., 2012; Slater, 2007) and hydraulic methods (Brauchler et al., 2003; Yeh and Liu, 2000; Zhu and Yeh, 2005), including tracer-based measurements (Doro et al., 2015; Jiménez et al., 2016; Somogyvári and Bayer, 2017), have been developed and employed for characterizing hydraulic properties (Lochbühler et al., 2013). In hydraulic flow methods, head data responses to hydraulic perturbations (pumping, tidal fluctuation, etc.) are measured at different locations across the aquifer. The recorded head data are then used to estimate the spatial distribution of hydraulic conductivity (K) and storativity. A distinct advantage of hydraulic methods for imaging purposes is that the hydraulic response of an aquifer is directly related to its hydraulic parameters described by flow equations (Fakhreddine et al., 2016), while in most geophysical methods, the hydraulic properties are inferred from other estimated physical properties, thereby, requiring petrophysical relationships. We define $Y=\log_{10}(K)$ and assume that is can be described by a stationary multivariate Gaussian distribution.

Hydraulic tomography has been the subject of many theoretical and numerical (Fienen et al., 2008; Luo et al., 2020; Yeh and Liu, 2000; Zha et al., 2018; Zhu and Yeh, 2005), laboratory (Illman et al., 2008, 2010; Liu et al., 2002, 2007; Yin and Illman, 2009; Zhao et al., 2016)), and field studies (Berg and Illman, 2015, 2013, 2011; Bohling et al., 2007; Brauchler et al., 2013, 2011, 2010, 2003; Cardiff et al., 2009, 2013; Cardiff and Barrash, 2011; Fischer et al., 2017; Gottlieb and Dietrich, 1995; Huang et al., 2011; Klepikova et al., 2013; Kuhlman et al., 2008; Paradis et al., 2016, 2015; Sun et al., 2013; Tosaka et al., 1993). However, hydraulic tomography based on head data alone has limitations. One limitation is inherent to the underlying potential-field physics as measured head data are spatially averaged due to the diffusive nature of pressure disturbances created during the test (Bohling and Butler Jr, 2010). This averaging results in tomographic estimates displaying a high degree of smoothing compared to the actual aquifer property fields. This smearing may lead to degraded predictions for transport problems. Another limitation appears in applying hydraulic tomography in high conductivity aquifers as hydraulic tests lead to small drawdown values, implying high relative uncertainty of the measured head perturbations and correspondingly low signal-to-noise ratio data. Adding other types of non-redundant data in hydraulic tomography can help to better image the subsurface (Mao et al., 2013; Yeh et al., 2015). In this regard, Zha et al. (2014) demonstrated the usefulness of flux data (specific discharge) for hydraulic tomography in a 2D synthetic fractured media mimicking a field site in Mizunami, Japan. Estimated mean, variance, and correlation length of the *Y*-field were applied as prior information to the inversion model. Using the cross-correlation approach (Zha et al., 2014), they showed that head and flux contribute differently to the *Y*-field reconstruction. They claimed that inversion of head data collected with known pumping rate can result in representative *Y*-field estimates even if the initial guess is incorrect. For flux data, they find that the final *Y*-field estimate is dependent on the initial guess. Their synthetic work showed that using flux data with head data improves the estimation of *Y*-field values and the fracture distribution. In another study, Tso et al.(2016) performed numerical test studies on a 3D model mimicking the aquifer at the North Campus Research site in Waterloo, Canada. They simulated pumping in this porous aquifer and measured head data and flux data at different locations. Then, head and flux data were subjected to inversion, considering different types of prior information. They showed that using flux data jointly with head data can enhance hydraulic conductivity estimates. Furthermore, they found out that the estimated hydraulic conductivity field is less affected by an inadequate prior model when non-redundant flux data are used to supplement the head data.

Until recently, measurements of groundwater fluxes in the field were limited to local and time-consuming measurements. The most popular technique for quantifying groundwater flux in the field was based on dilution tests (Drost et al., 1968; Jamin et al., 2015; Schneider et al., 2019), where the dilution of an injected tracer inside a screened borehole or within packers is used to estimate the horizontal groundwater flux. Nevertheless, boreholes disturb the flow field and affect the measurements; hence, the measured values may not represent the real flux values. The recent advent of Fiber Optic Distributed Temperature Sensors (FO-DTS) has led to new possibilities for measuring groundwater discharge with unprecedented spatial and temporal resolutions (des Tombe et al., 2019; Simon et al., 2021)

FO-DTS is a distributed sensor type that allows measurements of temperature all along the fiber optic cable. FO-DTS can be employed in both passive and active modes. In passive mode, the temperature of the fiber optic is measured without any external forcing, while in active mode, a heat source is added to the fiber optic cable by using a heating element located very close to the fiber optic cable or by using a heating fiber optic cable. Active-DTS have been developed, for instance, for measuring borehole flows (Read et al., 2014), wind speed (Sayde et al., 2015), and for characterizing groundwater fluxes in fractured media (Maldaner et al., 2019). Recently, it has also been used for measuring groundwater discharge in sedimentary aquifers; the FO cable typically being installed by the direct push method (Bakker et al., 2015; des Tombe et al., 2019). In this case, the buried cable is in direct contact with the ground with minimum subsurface perturbations. Simon et al. (2021) showed that active-DTS can be used for measuring both thermal conductivities and groundwater fluxes on a large range of values with excellent accuracy (with errors of less than 10% for groundwater flux in the range of 10^{-5} to 10^{-3} m/s). The principle of such an experiment (Figure 1) is to monitor the temperature evolution with time, which depends on the surrounding area's thermal properties and also groundwater fluxes that limits the temperature rise. Typically, the slope of the temperature rise in the conduction regime (with time in logarithmic scale) is inversely proportional to thermal conductivity while the greater the groundwater fluxes, the lower the temperature at stabilization. The temperature evolution with time may be easily interpreted to estimate groundwater fluxes through an analytical solution or by using a graphical analysis (Simon et al., 2021). The application of Active FO-DTS for flux measurements is currently limited to shallow and unconsolidated aquifers due to limitations in deployment by the direct push method.

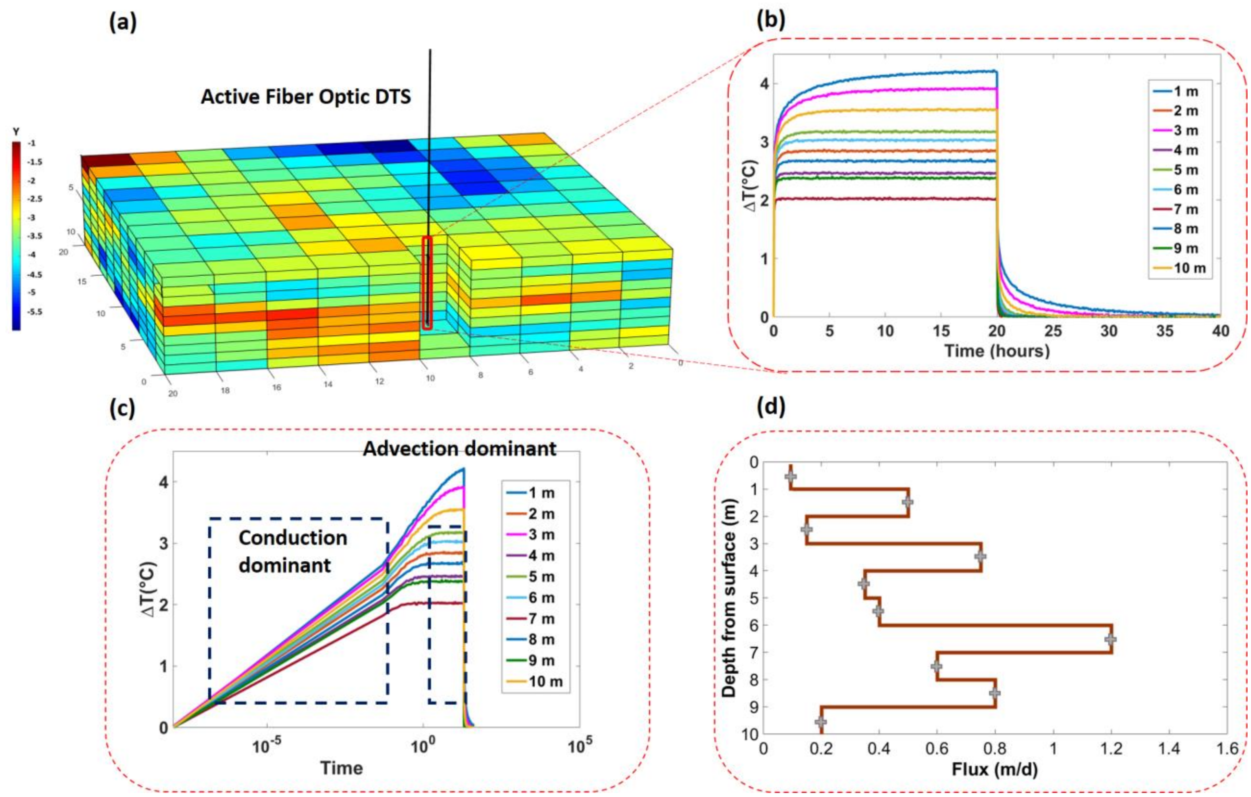

Figure 1: Schematic description of how Active FO-DTS can be used to infer a groundwater flux profile with depth. **(a)** An Active Fiber Optic Cable is deployed vertically into the ground in close contact with the formation. **(b)** The cable is heated (active mode), and the cable temperature during the heating (first 20 hours) and cooling periods (from 20 to 40 hours) is measured. Each curve corresponds to one-point measurement along the FO-cable. **(c)** In semi-logarithmic plot, the slope of the temperature profile is used to estimate the thermal conductivity while the temperature at stabilization is dependent on groundwater fluxes (Simon et al., 2021). **(d)** Measured temperature data along the fiber optic cable are converted to a flux profile with depth, with each "+" sign indicate one datum.

New advances in distributed sensing of groundwater flux make it an appealing data source for independent inversion or joint inversion with hydraulic head. This present study assumes that groundwater fluxes can be inferred from such above-mentioned techniques at a prescribed spatial resolution and accuracy. Here, we limit ourselves to a 2-D study assuming constant groundwater flux in depth. Using a geostatistical hydraulic tomography approach, we then address the benefits and drawbacks of using either head or flux data individually or jointly. More specifically, we address the following questions.

(1) For an equal number and locations of flux and head data, which data type leads to the best reconstruction of hydraulic conductivity?

(2) How does the number of observations affect the inversion results?

(3) How does inversion performance for the different data types vary with the hydraulic conductivity field variance?

The paper is structured into six sections. Section 2 presents the geostatistical inversion method and the forward model employed. In section 3, we describe the hydraulic conductivity test model used for our analysis. In sections 4 and 5, we present and discuss the main results, respectively, and section 6 concludes the paper.

2. METHODS

The Principal Component Geostatistical Approach (PCGA) is a computationally-efficient geostatistical inversion method (Lee and Kitanidis, 2014). PCGA uses the main principal components of the prior model covariance matrix for model parameterization and corresponding estimates of the Jacobian (sensitivity matrix). The resulting model reduction from a model of many gridded elements to a lower number of retained principal components leads to smaller matrices to invert and fewer sensitivities to estimate, implying less computational costs than full inversions. This method has been employed extensively in recent years (Fakhreddine et al., 2016; Fischer et al., 2017; Kang et al., 2017; Lee et al., 2018; Soueid Ahmed et al., 2016). In this study, we use PCGA combined with the Matlab Reservoir Simulation Toolbox (MRST) that simulates fluid flow in porous media (forward model) to perform inversion of head and flux data.

2.1 Inverse model

Inferring properties of subsurface media (storage, hydraulic conductivity) from error-contaminated and sparse observed data (head data, flux data, etc.) is an inverse problem and can be formulated as follow:

$$\mathbf{d} = f(\mathbf{m}) + \boldsymbol{\eta}, \tag{1}$$

where $\mathbf{d}$, f(-), $\mathbf{m}$ and $\boldsymbol{\eta}$ refer to measured data, forward model, model parameters and errors, respectively. The forward model refers here to a non-linear operator solving a set of differential equations numerically to describe the relationship between model parameters and data. From a mathematical point of view, the inverse problem is often ill-posed and the solution is non-unique, implying that additional information (e.g., a prior model) is required to obtain unique and physically-meaningful results. Here, the subsurface is described as a multi-Gaussian stationary field with known statistical properties and a superimposed deterministic trend. In the presence of a multivariate Gaussian prior model and error distribution, it is common to formulate the inverse problem in terms of an exploration of the maximum a posteriori (MAP) estimate and its variance. In such a setting, the solution of the inverse problem is obtained by maximizing a posterior probability density function (maximizing the term in bracket) expressed by using Bayes' theorem as follow:

$$\pi_{post}(\mathbf{m}|\mathbf{d}) \sim \exp[\tfrac{-1}{2}(f(\boldsymbol{m}) - \mathbf{d})\mathbf{C}_{\mathrm{d}}^{-1}(f(\mathbf{m}) - \mathbf{d}) + \tfrac{-1}{2}(\mathbf{m} - \mathbf{m}_{\mathrm{prior}})\mathbf{C}_{\mathrm{m}}^{-1}(\mathbf{m} - \mathbf{m}_{\mathrm{prior}})] , \tag{2}$$

where $\mathbf{C_m}$ and $\mathbf{C_d}$ are the a priori model covariance and data covariance matrix, respectively (Kitanidis, 1995).

Geostatistical methods have been widely used and proven to be efficient for hydraulic tomography purposes (Illman et al., 2015). The iterative optimization process estimates the model parameters. The solution at $(i+1)^{\mathrm{th}}$ iteration is calculated as:

$$\mathbf{m}_{i+1} = \mathbf{X}\boldsymbol{\beta}_i + \mathbf{C}_{\mathrm{m}}\mathbf{J}_i^{T}\boldsymbol{\varepsilon}_i , \tag{3}$$

where $\mathbf{X}$ is a known matrix, and $\boldsymbol{\beta}$ is an unknown vector used to determine linear trends that is inferred along with $\boldsymbol{\varepsilon}$ by solving the system of equations below. Here $\mathbf{J}$ represents the Jacobian matrix describes the sensitivity of the forward model output (at observation points) with respect to the unknown model parameters.

$$\begin{bmatrix} \mathbf{J}_i\mathbf{C}_\mathrm{m}\mathbf{J}_i^{T} + \mathbf{C}_\mathrm{d} & \mathbf{J}_i\mathbf{X} \\ (\mathbf{J}_i\mathbf{X})^{T} & 0 \end{bmatrix} \begin{bmatrix} \boldsymbol{\varepsilon}_i \\ \boldsymbol{\beta}_i \end{bmatrix} = \begin{bmatrix} \mathbf{d} - f(\mathbf{m}_i) + \mathbf{J}_i\mathbf{m}_i \\ 0 \end{bmatrix}. \tag{4}$$

2.1.1 Principal Component Geostatistical Approach

Calculating the Jacobian matrix (**J**) used in equations (3) and (4) for high-dimensional problems often requires a very high computational effort. Lee and Kitandis (2014) proposed the Principal Component Geostatistical Approach (PCGA), which uses a low-rank approximation of the prior covariance via principal component analysis and avoids forming the Jacobian explicitly for products of the Jacobian matrix and eigenvalues (equations (6) and (7)) by using a finite difference approximation (equation (8)). This results in a faster inversion process of high accuracy, provided that an adequate number of principal components are retained. The terms that are used for geostatistical inversion in equation (4) are approximated through the P largest principal components as follow:

$$\mathbf{C}_\mathrm{m} \approx \mathbf{C}_{\mathrm{m}P} = \sum_{ii=1}^{P} (\varsigma_{ii})(\varsigma_{ii})^{T}, \tag{5}$$

$$\mathbf{J}_i\mathbf{C}_\mathrm{m} \approx \mathbf{J}_i\mathbf{C}_{\mathrm{m}P} = \mathbf{J}_i \sum_{ii=1}^{P} (\varsigma_{ii})(\varsigma_{ii})^{T} = \sum_{ii=1}^{P} (\mathbf{J}_i\varsigma_{ii})(\varsigma_{ii})^{T}, \tag{6}$$

$$\mathbf{J}_i\mathbf{C}_\mathrm{m}\mathbf{J}_i^{T} \approx \mathbf{J}_i\mathbf{C}_{\mathrm{m}P}\mathbf{J}_i^{T} = \sum_{ii=1}^{P} (\mathbf{J}_i\varsigma_{ii})(\mathbf{J}_\mathrm{i}\varsigma_{ii})^{T}, \tag{7}$$

$$\mathbf{J}_i\varsigma_{ii} \approx \frac{1}{\delta}[f(\mathbf{m}_i+\delta\varsigma_{ii})\text{-}f(\mathbf{m}_i)]\,. \tag{8}$$

Here, $\mathbf{C}_{\mathrm{m}P}$ is a rank-P approximation of the model parameter covariance matrix. The C_{mP} and Jacobian matrix products required for the inversion (equation 4) are given by equations 6-7. How to choose the finite difference interval δ is addressed by Lee and Kitandis (2014).

The diagonal entries of the posterior covariance matrix ($\mathbf{v}_{jj}$) are often presented as the estimation of the variance and can be calculated without explicit construction of **v** (Lee and Kitanidis, 2014)

$$\mathbf{v}_{\mathrm{jj}} = \mathbf{C}_{\mathrm{m}\,jj} - \begin{bmatrix} (\mathbf{JX})_j \\ \mathbf{X}^T \end{bmatrix}^T \begin{bmatrix} \mathbf{JC}_{\mathrm{m}}\mathbf{J}^T + \mathbf{C}_{\mathrm{d}} & \mathbf{JX} \\ (\mathbf{JX})^T & 0 \end{bmatrix}^{-1} \begin{bmatrix} (\mathbf{JX})_j \\ \mathbf{X}_j{}^T \end{bmatrix}, \tag{9}$$

where $\mathbf{C}_{\mathrm{m}jj}$ represents the j^{th} diagonal entry of the model covariance matrix and $(\mathbf{JX})_j$ is the j^{th} column of the product $\mathbf{JX}$.

Once the model parameters are determined, it is desirable to perform a resolution analysis by obtaining the resolution matrix ($\mathbf{R}$), which can be seen as a low pass filter that maps the true model parameters to the estimated model parameters (e.g., Alumbaugh and Newman, 2000). Each model parameter during the inversion is estimated from the averaging of other model parameters adjacent to the one of interest. The components of $\mathbf{R}$ can be interpreted as weights (each row in the resolution matrix) of the average of true model parameters for estimating each model parameter (Day- Lewis et al., 2005). The ideal resolution matrix would be an identity matrix that would imply that all model parameters are resolved perfectly. The deviation of the diagonal element from the identity matrix reveals the degree of averaging and smoothness. Thus, plotting diagonal elements of the resolution matrix in their corresponding blocks is indicative of the degree of smoothness. The diagonal elements of the resolution matrix (equation 11) inform the extent to which each estimated parameter is resolved independently.

The resolution matrix ($\mathbf{R}$) is obtained by equation (11), which requires recovering the Jacobian matrix ($\mathbf{J}_{\mathrm{r}}$) from the previously calculated product (equation 6) and inverse of low rank-approximation of the covariance matrix ($\mathbf{C}_{\mathrm{m}P}$) as shown in equation (12);

$$\mathbf{m}^{\mathrm{estimate}} = \mathbf{R}\mathbf{m}^{\mathrm{true}}, \tag{10}$$

$$\mathbf{R} = (\mathbf{J}_{\mathrm{r}}{}^T(\mathbf{C}_{\mathrm{d}})^{-1}\mathbf{J}_{\mathrm{r}})^{-1}(\mathbf{J}_{\mathrm{r}}{}^T(\mathbf{C}_{\mathrm{d}})^{-1}\mathbf{J}_{\mathrm{r}}). \tag{11}$$

$$\mathbf{J}_{\mathrm{r}} = \left(\sum_{\mathrm{ii}=1}^{P} (\mathbf{J}_i\varsigma_{ii})(\varsigma_{ii})^T\right)\left(\sum_{ii=1}^{P} (\varsigma_{ii})(\varsigma_{ii})^T\right)^{-1} \tag{12}$$

It should be noted that $\mathbf{J}_{\mathrm{r}}$ is the Jacobian matrix mapped from the PCA space to the grid cells, while $\mathbf{J}$ is the Jacobian matrix calculated directly for every principal component.

2.2 Forward model

The incompressible fluid flow module of MRST (Lie, 2019) was used to simulate steady-state groundwater flow. It is used to calculate head and flux values at different points across a confined aquifer. Starting from the mass conservation law on a control volume, introducing the Darcy law, assuming incompressible fluid flow and steady-state condition, the final form of the equation reads:

$$-\nabla.[\boldsymbol{K}(\mathbf{w}).\nabla h(\mathbf{w})] = \mathbf{q}(\mathbf{w})\,, \tag{13}$$

subjected to the following constant head boundary conditions across external boundaries:

$$h{=}h_{\mathrm{D}} \quad \text{for} \quad \vec{\mathbf{w}} \in \Gamma_{\mathrm{a}} \tag{14}$$

Here, $\mathbf{w}= (x, y, z)$, K (L/T), h (L) and $\mathbf{q}$ [L/T] represent the hydraulic conductivity, head and fluid source or sink (inflow or outflow of fluid per volume at certain locations), respectively. Γ_{a} represents Dirichlet boundaries. The above equations are solved numerically to calculate the head values at grid points across the aquifer. The MRST uses the two-point flux approximation scheme (Lie, 2019) to calculate the Darcy flux in each grid block.

3. NUMERICAL EXPERIMENTS

3.1 Setup of the synthetic test case

To assess the information content of hydraulic head and groundwater flux data for the reconstruction of heterogeneous aquifers, a stationary multi-Gaussian log-hydraulic conductivity field (with constant storativity) is generated, resulting in the field, shown in Figure 2. The generated aquifer is 550 m in length, 550 m in width and 5 m in depth. The aquifer is discretized into 110 × 110 × 1 in x-, y-, z- directions and corresponding block sizes are 5 m × 5 m × 5 m, respectively. The aquifer is assumed to have one layer, and the log-hydraulic conductivity field has a multi-Gaussian distribution. The area of interest is chosen in the middle of the aquifer, away from the boundaries to reduce the boundaries' effect on the inversion. All boundaries are set to a constant head equal to 350 m.

The correlation length used for generating the *Y*-field is 75 m and 45 m for *x*- and *y*-directions, respectively. The same field (same heterogeneity structure) with different variances of 0.5, 1, 2, and 4 are generated to assess the effect of variance and number of observations on the inversion results. The mean Y_{mean} is -3.57 for all cases, but the *Y*-fields variance and ranges are different for different experiments. This range of hydraulic conductivity is chosen to have measurable and realistic groundwater flux and head responses.

We use a five-spot setup with a central borehole (P1) and four boreholes (P2, P3, P4 and P5) on the corners of the area of interest (bounded by white dashed lines in Figure 2). Other monitoring points are also considered between the boreholes, as shown by asterisk symbols. The aquifer is subjected to a series of pumping experiments in each borehole. Two different boundary conditions in the borehole, namely, constant rate and constant head, are considered. When simulating pumping in one borehole, the head and flux values are recorded in other boreholes and monitoring points. The acquired flux and head data are noise-contaminated before being used to estimate the *Y*-field.

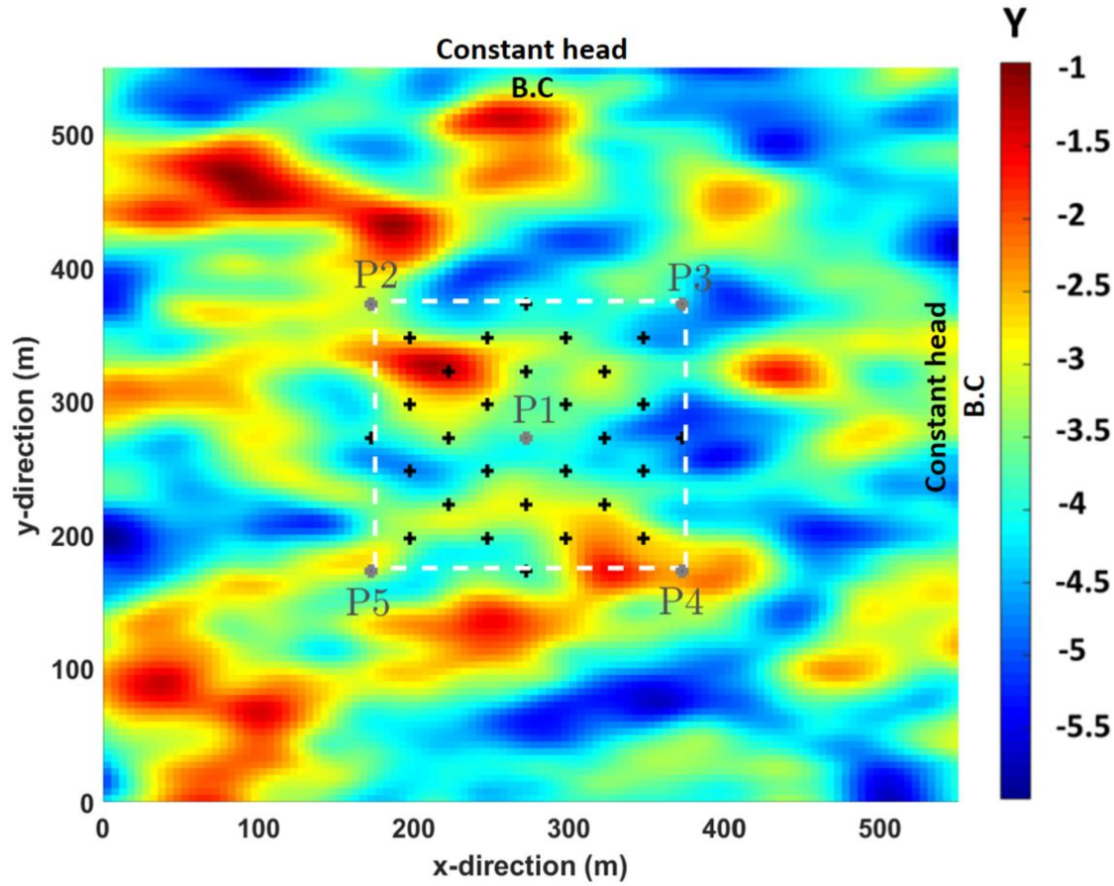

Figure 2: Reference *Y*-field (variance 4), borehole (P1 to P5), and monitoring locations (asterisks). All boundaries are set to the constant head. The white dash-lines crossing the side boreholes define the area of interest.

3.2 Hydraulic tomography using head and flux data

Our numerical inversion experiments aim to compare the relative merits of each data type and analyze how borehole boundary conditions (constant head or constant rate), the variance of the *Y*-field, and the number of observations affect the inversion results. The observational data are generated using the reference hydraulic conductivity field, and a normally distributed and independent error is added to the observations. The standard deviations of these errors are different in all cases. The errors' standard deviations were chosen to be in a realistic range while ensuring the same initial signal-to-noise ratio of 38 for all cases defined by running the code using Y_{mean}. The resulting measurement errors range from 0.05 to 0.013 (m) for the head and 0.055 to 0.01 (m/day) for the flux.

PCGA with previously mentioned geostatistical parameters are used for the inversion. The truncation order (*p*-rank) of the prior covariance matrix is chosen as 400 out of 12100. Based on the recommendation by Lee et al. (2016), the truncation order (P), which results in the relative Eigenvalue error below 0.01 would be sufficient to capture most of the covariance matrix structure. The relative Eigenvalue error is defined as the ratio of first to (P+1)th Eigenvalue. We have chosen P more conservatively. For the Y-field with variance 4, the first Eigenvalue is 1411.47, while the 401st Eigenvalue is 0.047 giving the ratio of 3.25×10^{-5}.

The inversion starts with a constant value of Y_{mean} and continues until the root mean square error between observed and simulated measurement, normalized with the error standard deviation (weighted root mean square error), defined in equation 15 reaches a value close to one,

$$\mathrm{WRMSE}=\sqrt{\frac{\frac{1}{N}\sum_{1}^{N}(\mathbf{d}\text{-}f(\mathbf{m}^{\mathrm{estimate}}))^2}{\sigma^2}}, \qquad (15)$$

here N is the number of observations and σ is the absolute value of the error's standard deviation. If no convergence is obtained, the inversion ends after 10 iterations.

3.2.1 Boundary condition at the pumping borehole

Hydraulic tomography is simulated considering two different borehole boundary conditions: constant rate (the borehole is being pumped with constant flow rate) and constant head (the head in the borehole is kept constant). Note that the external boundary conditions do not change and are kept fixed. As an example, the pumping rates for the field case with variance 4 are 2400, 4000, 1750, 5000, and 3800 (m^3/day) for P1, P2, P3, P4, and P5, respectively. The equivalent constant head borehole boundary conditions are 324, 340, 300, 329 and 336 (m) for P1, P2, P3, P4, and P5, respectively.

3.2.2 Variance of *Y*-field and number of observation points

The effect of the Y-field variance is investigated by considering four different variances (0.5, 1, 2 and 4). Furthermore, a different number of observation points are used to assess their impact on the final inversion results. The observation points are distributed symmetrically in the aquifer. The minimum number of observation points considered is the number of boreholes (4 observation points) and the maximum are the boreholes and the observation points shown by asterisks in Figure 2 (32 observation points). We distinguish between the number of observations and the number of observation points. For head and flux data, the number of observation points and number of observations are the same. For joint inversion, the number of observations is twice the number of observation points.

3.3 Performance Metrics

To evaluate each data type's performance in estimating Y, we use the Frobenius norm and scatter plots of estimated versus reference Y for each case. The Frobenius norm for the vector of difference between the reference Y and estimated Y is:

$$\mathrm{Norm}^{\mathrm{Fr}} = \sqrt{\sum_{1}^{N} \left| \mathbf{Y}_{\mathrm{reference}} - \mathbf{Y}_{\mathrm{estimated}} \right|^{2}}, \tag{16}$$

Furthermore, the correlation coefficient between reference Y and estimated Y-values and their corresponding slope lines are calculated.

4. RESULTS

4.1 Inversion of head data

First, the head data are individually inverted. The results are presented for 4 observation points (only the observations in the boreholes), 8, 16 and 32 observation points. For each case, two different borehole boundary conditions are considered: constant rate and constant head. Figure 3 shows the estimated Y-field with a variance of 4, and Table 1 represents the performance metrics.

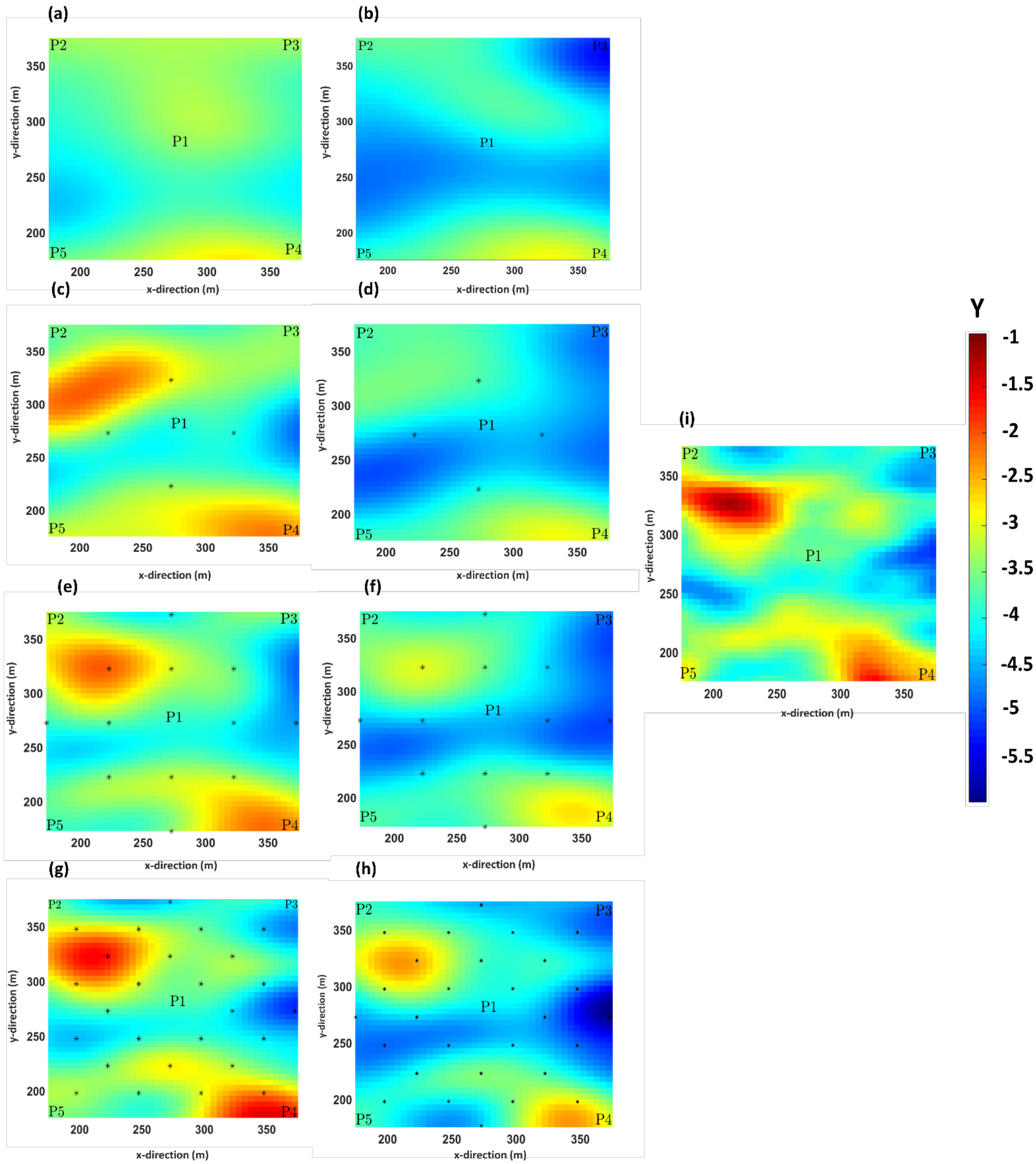

Figure 3: Hydraulic conductivity field (variance 4) estimates from hydraulic head data: **(a)** inversion result for 4 observations point and constant rate B.C., **(b)** inversion result for 4 observations point and constant head B.C., **(c)** inversion result for 8 observations point and constant rate B.C., **(d)** inversion result for 8 observations point and constant head B.C., **(e)** inversion result for 16 observations point and constant rate B.C., **(f)** inversion result for 16 observations point and constant head B.C., **(g)** inversion result for 32

observation points and constant rate B.C., **(h)** inversion result for 32 observation points and constant head B.C. **(i)** reference *Y*-field

Table 1: Performance metrics (in the area of interest) from the inversion of head data for the case of a *Y*-variance of 4.

Variance	Boundary Condition	Number of observations	Frobenius norm	Correlation coefficient	Slope	Final WRMSE
4	Constant Rate	4	68.4	0.27	0.13	1.19
		8	48.27	0.75	0.62	1.05
		16	30.4	0.9	0.76	0.97
		32	23.47	0.94	0.95	1.1
	Constant Head	4	85.5	0.49	0.32	1.00
		8	75.15	0.68	0.48	0.96
		16	61.9	0.82	0.67	1.26
		32	54.90	0.9	0.93	1.23

For all cases, we find that changing the borehole boundary condition from constant rate to constant head deteriorates the *Y*-field estimation. This is quantified by the fact that the Frobenius norm (Table 1) increases from 68.4 to 85.5, 48.27 to 75.15, 30.4 to 61.9 and 23.47 to 54.90 for 4, 8, 16 and 32 observation points, respectively. Comparing Figures 3(a) to 3(h) with the reference *Y*-field (Figure 3 (i)) also show that cases with constant rate boundary conditions is visually closer to the reference *Y*-field. The use of constant head borehole boundary condition results in an underestimation of *Y*-field values and the mean value of *Y*-field. For instance, in the case of 4 observation points, the mean value of the estimated *Y*-field is around -4 for constant head boundary condition while it is -3.45 for constant rate boundary condition. The mean value of the reference *Y*-field is -3.57. Adding more observations leads to better results. This is reflected in the improvement of the correlation coefficient from 0.27 to 0.94 for constant rate borehole boundary condition and from 0.49 to 0.93 for constant head boundary condition when adding observation points. Associated increases in the slopes from 0.13 to 0.95 and from 0.32 to 0.93 for constant rate and constant head boundary conditions further underline the previous statement.

4.2 Inversion of flux data

We now consider the results obtained by individual inversions of flux data for a *Y*-field variance of 4. Figure 4(a) to (h) show the *Y*-field estimates for 4, 8, 16 and 32 observation points subjected to constant rate and constant head borehole boundary conditions. Table 2 provides the corresponding performance metrics.

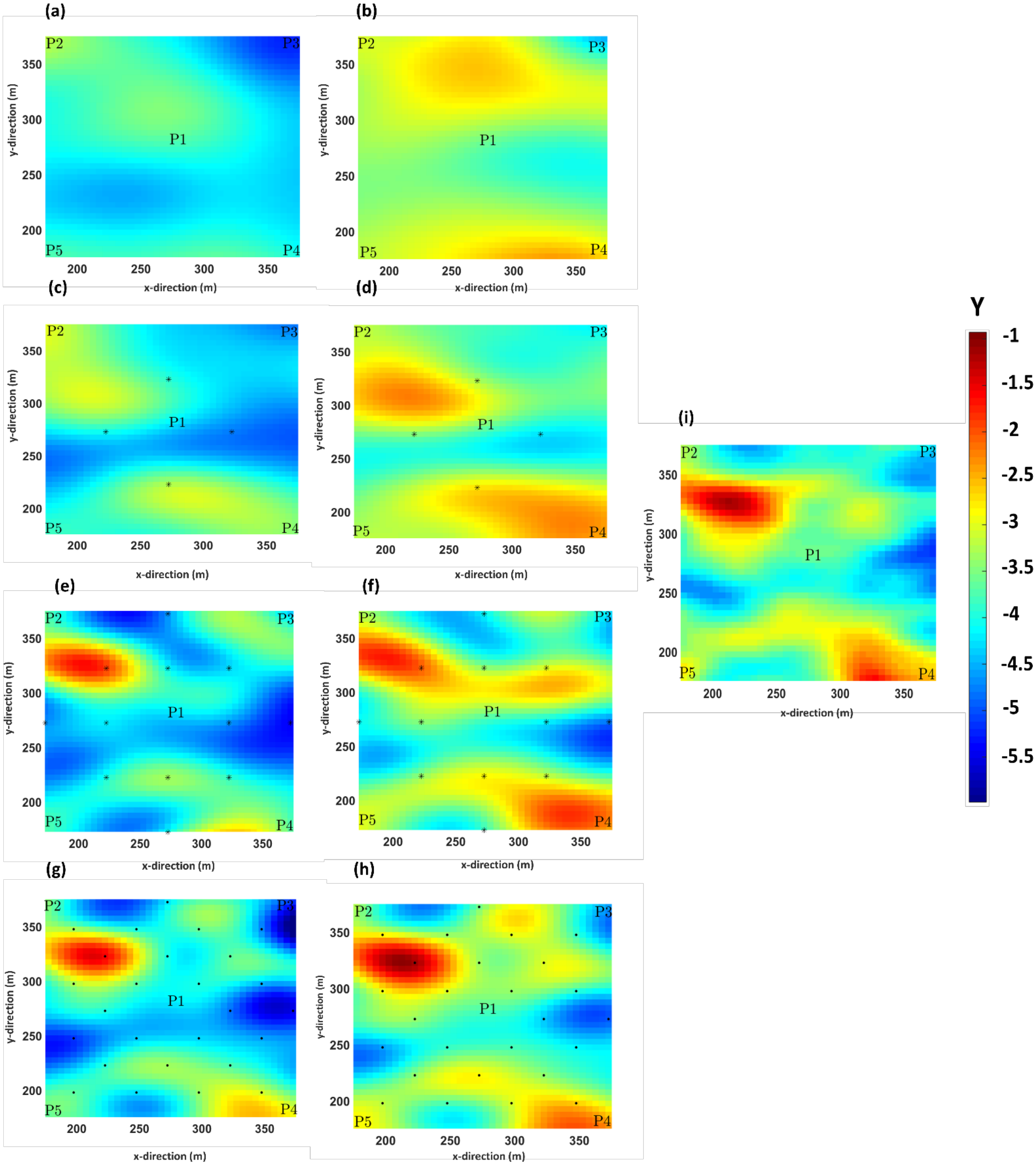

Figure 4: Hydraulic conductivity field (variance 4) estimates from flux data: **(a)** inversion result for 4 observations point and constant rate B.C., **(b)** inversion result for 4 observations point and constant head B.C., **(c)** inversion result for 8 observations point and constant rate B.C., **(d)** inversion result for 8

observations point and constant head B.C., **(e)** inversion result for 16 observations point and constant rate B.C., **(f)** inversion result for 16 observations point and constant head B.C., **(g)** inversion result for 32 observation points and constant rate B.C., **(h)** inversion result for 32 observation points and constant head B.C., **(i)** reference *Y*-field

Table 2: Performance metrics (in the area of interest) from the inversion of flux data for the case of a *Y*-variance of 4.

Variance	Boundary Condition	Number of observations	Frobenius norm	Correlation coefficient	Slope	Final WRMSE
4	Constant Rate	4	81.2	0.45	0.22	1.31
		8	65.61	0.76	0.56	1.19
		16	62.2	0.79	0.77	1.34
		32	53.6	0.9	0.90	2.12
	Constant Head	4	64.53	0.53	0.29	1
		8	47.7	0.77	0.61	1
		16	44.72	0.8	0.81	0.95
		32	32.03	0.92	0.91	1.45

Contrary to head data, we find that constant head boundary conditions provide a better *Y*-field estimate when considering flux data. The better performance of the constant head (with respect to constant rate) boundary condition is seen, for instance, by comparing the values of the Frobenius norm given in Table 2. For the case of 4, 8, 16, and 32 observation points, the Frobenius norm decreases from 81.2 to 64.53, 65.61 to 47.7, 62.2 to 44.7, and from 50.51 to 32.03, respectively. Using constant rate boundary condition for the flux data results in an underestimation of the *Y*-field mean. Considering the case with 4 observation points, the estimated *Y*-field's mean value with the constant rate boundary condition is around -4 while it is around -3.4 for the constant head boundary condition.

Comparing the values of Frobenius norm for the head and flux data given in Table 1 and Table 2 reveals that for a small number of observations (4 observation points), using flux data with constant head boundary condition gives a better *Y*-field estimate compared to head data with constant rate boundary condition as the Frobenius norm decreases from 68.4 to 64.53. This improvement is further supported by an increase in the correlation coefficient from 0.2744 to 0.446 and slope increase from 0.127 to 0.22. For a larger number of observations, the performance of the two data types is similar when considering their ideal boundary conditions.

4.3 Joint Inversion of flux and head data

The results obtained by joint inversion of flux and head data are provided in Figure 5 (a) to (h) that show the *Y*-field estimate for 8, 16, 32, and 64 observations subjected to the constant head and constant rate borehole boundary conditions. The inversion metrics are outlined in Table 3. It should be noted that we have two measurements (head and flux) for each point shown leading to 64 observations for 32 observation points for instance.

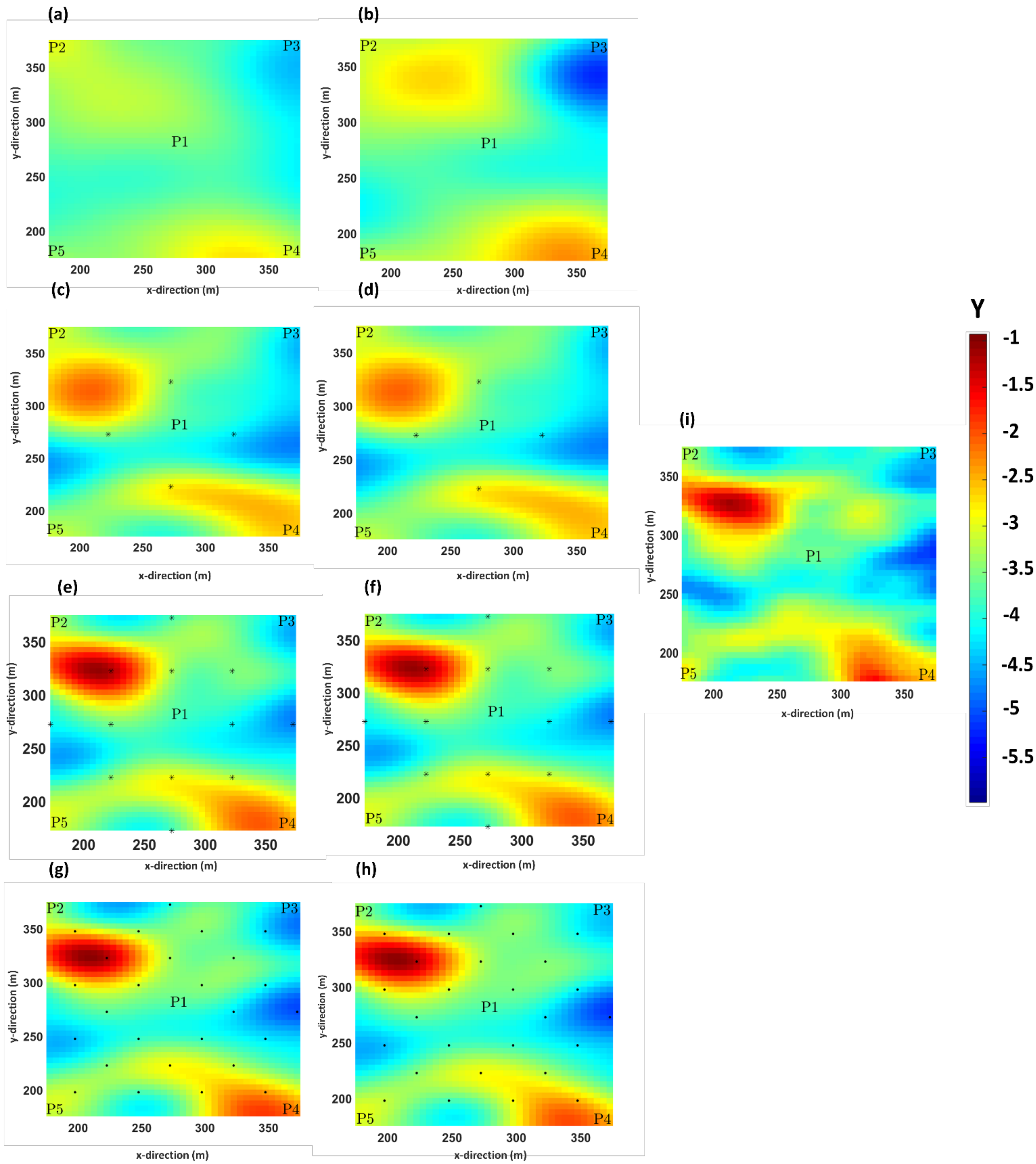

349

Figure 5: Hydraulic conductivity field (variance 4) estimates from joint inversion: **(a)** inversion result for 4 observations point and constant rate B.C., **(b)** inversion result for 4 observations point and constant head B.C., **(c)** inversion result for 8 observations point and constant rate B.C., **(d)** inversion result for 8 observations point and constant head B.C., **(e)** inversion result for 16 observations point and constant rate B.C., **(f)** inversion result for 16 observations point and constant head B.C., **(g)** inversion result for 32 observation points and constant rate B.C., **(h)** inversion result for 32 observation points and constant head B.C., **(i)** reference *Y*-field

Table 3: Performance metrics for joint inversion of head and flux data in the area of interest

Variance	Boundary Condition	Number of observations	Frobenius norm	Correlation coefficient	Slope	Final WRMSE
4	Constant Rate	8	51.8	0.7	0.34	0.8
		16	39.7	0.82	0.68	1.24
		32	24.44	0.94	0.92	2.25
		64	22	0.96	0.98	1.13
	Constant Head	8	53.97	0.64	0.51	1.1
		16	38.34	0.84	0.74	1.13
		32	27.38	0.93	0.92	1.5
		64	21.71	0.95	0.97	1.65

The Frobenius norms for 8, 16, 32 and 64 observations are 51.8, 39.7, 24.44 and 22, respectively, when considering constant head borehole boundary conditions, while they are 53.97, 38.34, 27.38 and 21.71 for constant rate boundary condition. For the same number of observations, the Frobenius norms are very similar regardless of borehole boundary conditions. In contrast to individual inversions, this suggests that they do not significantly affect the results obtained by joint inversion.

The joint inversion results (Table 3) do not demonstrate any significant improvement compared to the individual inversions (Tables 1 and 2) when considering the same number of observations. For 8 observations, the minimum Frobenius norm obtained for head, flux and joint inversion are 48.27, 47.7 and 51.8, respectively. For 16 observations, the minimum Frobenius norm obtained for head, flux and joint inversion are 30.4, 44.72 and 38.34, respectively while it is 23.47, 32.03 and 24.44 for 32 observations. When considering the same number of observation points, the joint inversion has twice as many observations as the individual inversions. This leads to significantly better estimates of the hydraulic conductivity field.

5. DISCUSSION

5.1 General findings

Considering the results of all 96 inversion scenarios considered, we find that inversion of flux data (with appropriate borehole boundary condition) leads to better resolved *Y*-field estimates then when considering head data particularly when a small number of observations are available. Furthermore, the quality of the inversion results is strongly dependent on the type of boundary condition used in the borehole. The performance metrics in Tables 1 and 2 suggest that it is more suitable to use constant rate borehole boundary condition for head data and constant head borehole boundary condition for the flux data as reflected in Frobenius norms' values. The reason is that if the observation is head data and the borehole boundary is set to constant head, the model response (head) will have less sensitivity to change of *Y*-field values. The same argument is also valid for the flux data.

The effect of the borehole boundary is essential for proper experimental design. The experimental designs should ensure that once head data are intended to be used for the inversion, wells must be pumped at a constant rate while for the inversion of the flux data, the head in the borehole should be kept fixed. Other borehole boundary conditions lead to an underestimation of hydraulic conductivity values. However, for the joint inversion of both data, the type of borehole boundary conditions does not play a significant role.

Tso et al. (2016) and Zha et al. (2014) found that joint inversion of head and flux data results in better estimation of *Y*-fields in porous and fractured media compared to the head data. Here, we find that joint inversion does not offer any advantage over the individual inversion of the flux and head data when considering an equal number of observations and ideal borehole boundary conditions. Our results rather suggest that, for a constant signal-to-noise-ratio, the inversion performance depends largely on the number of observations. For a small number of observations, the flux data provides a superior *Y*-field estimate compared to inversion of head data, while for the higher number of observations, all data types perform similarly. However, if we would be able to measure flux and head data at the same location, then for the same number of observation points, joint inversion of flux and head data provide better estimates of *Y*-field as the number of observations are doubled. Furthermore, we demonstrated the importance of borehole boundary conditions for hydraulic tomography experimental design when performing individual inversions.

A resolution analysis for the case of the variance of 4 and 4 measurement points demonstrates that flux data can better resolve the hydraulic conductivity field compared to head data (Figure 6). Figure 6 shows the diagonal elements of the resolution matrix (calculated in the final inversion iteration) for head data, flux data, and joint inversion of both data are plotted on their corresponding blocks, respectively. Considering the best *Y*-field estimates obtained for the head (constant rate boundary condition) and flux (constant head boundary condition) data for calculating the resolution matrices, as shown in Figure 6 (a) and 6 (d), it can be stated that model parameters (hydraulic conductivity values) are better resolved by flux data. This is manifested by comparing both the values and coverage area of diagonal elements larger than 0.005. When head data are used for the inversion, the degree of smoothing and averaging is higher compared to the case in which the flux data are used. It is worth noting that using the constant head boundary condition for head data can better resolve the *Y*-field heterogeneity structure than the constant rate boundary condition, even though it underestimates the *Y*-field values. Comparing Figure 6 (a) and 6 (b) and the correlation coefficient in Table 1 certifies this statement. The correlation coefficient increases from 0.27 to 0.49 when a constant head boundary condition is used instead of a constant rate boundary condition.

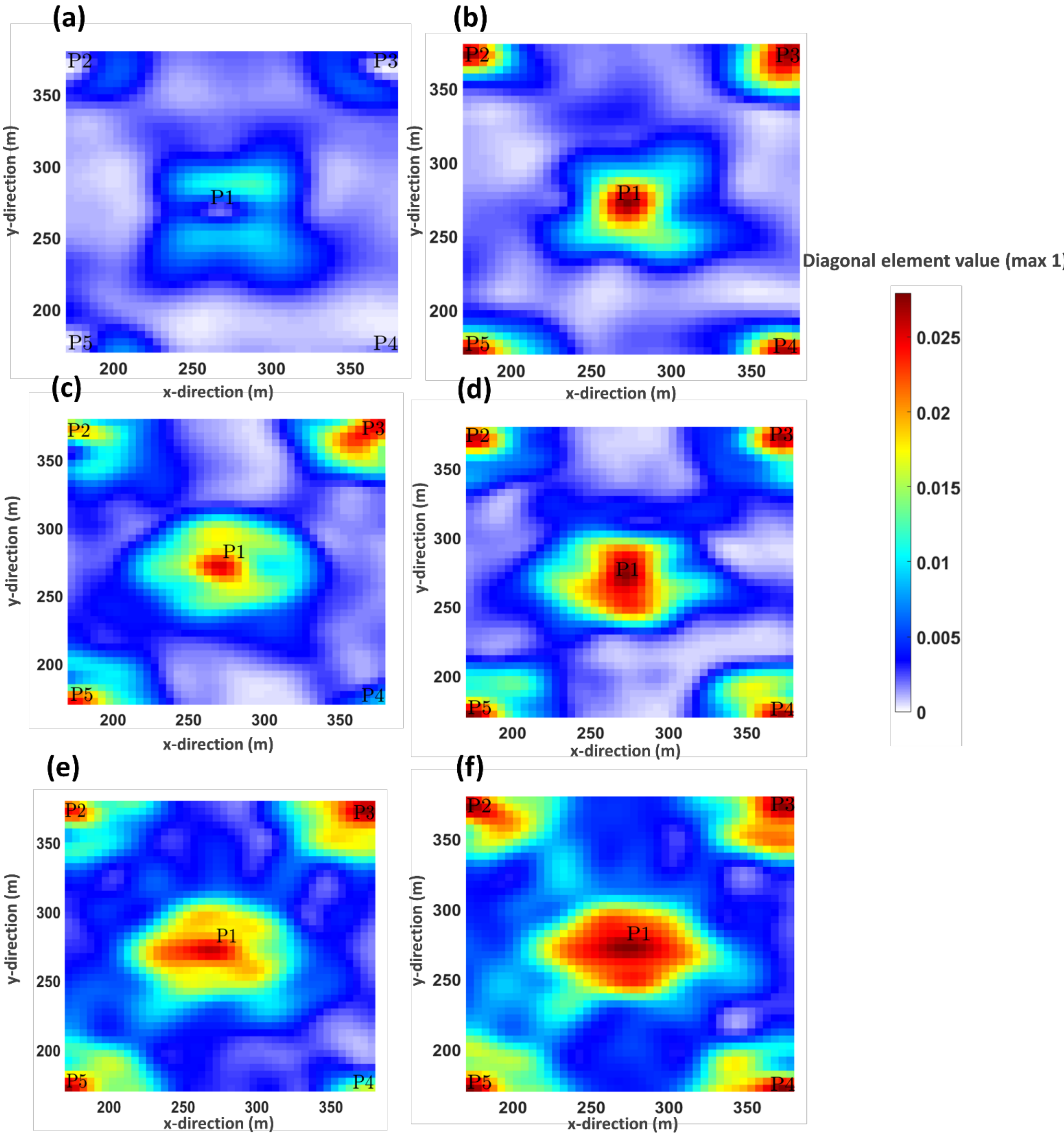

Figure 6: Diagonal element of the resolution matrix for **(a)** *Y*-field obtained by inversion of head data (4 observation points - borehole boundary is set to constant rate), **(b)** *Y*-field obtained by inversion of head data (4 observation points - borehole boundary is set to constant head**), (c)** *Y*-field obtained by inversion of flux data (4 observation points - borehole boundary is set to constant head), **(d)** *Y*-field obtained by inversion of flux data (4 observation points - borehole boundary is set to constant rate), **(e)** *Y*-field obtained by joint inversion of both data (4 observation points - borehole boundary is set to constant rate),

(f) *Y*-field obtained by joint inversion of both data (4 observation points - borehole boundary is set to constant rate).

5.2 The effect of number of observations and variance

Figures 7 (a) to (d) show the correlation coefficient (between estimated *Y*-field and reference *Y*-field) versus the number of observations for different type of data and borehole boundary conditions. It is seen that as the number of observations increases, the correlation coefficient also increases for all types of data and boundary conditions. For a small number of observations, flux data are superior to head data. The difference between the correlation coefficient of flux and head data is the strongest for a small number of observations, while the difference gradually decreases as the number of observations increases and at a high number of observations, they converge. This is a consequence of the decreasing distance between data points as the number of observations increases, thereby decreasing the radius of averaging. The gains by joint inversion for a prescribed number of observation points is that performance is independent of the borehole boundary condition and we need half as many boreholes if we are able to measure head and flux data at the same location.

The variance of the hydraulic conductivity field affects the final values of the correlation coefficient. The higher the variance, the lower the correlation coefficient (especially for a small number of observations), and also the more challenging it is to reach a WRMSE close to 1.

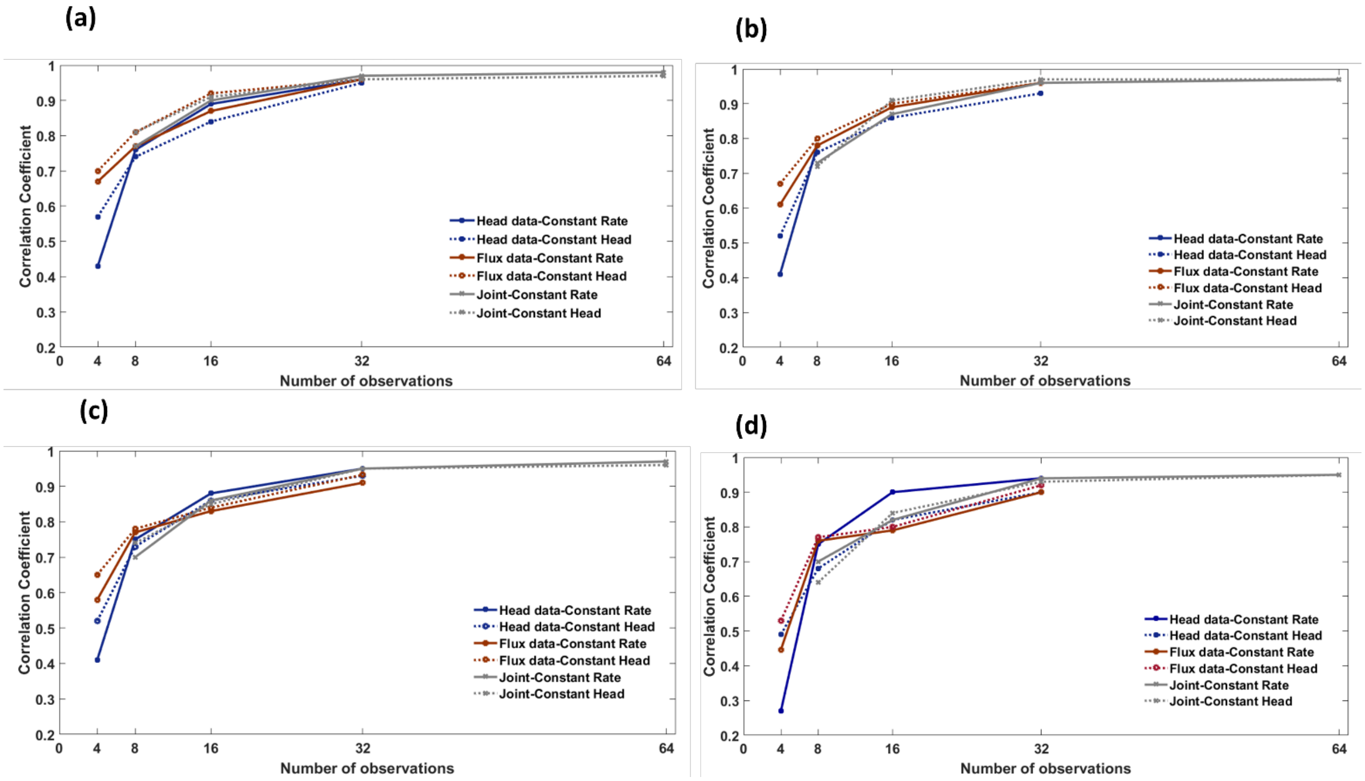

Figure 7: Correlation coefficient versus number of observations for reference hydraulic conductivity field with **(a)** variance=0.5, **(b)** variance=1 **(c),** variance=2 **(d),** variance=4. The Blue, red and gray color show the results for head data, flux data and joint inversion of both data, respectively. The data with constant rate borehole boundary condition is marked with solid line while the data with constant head borehole boundary condition is shown by the dashed line.

5.3 The effect of truncation order (*P*) on final inversion results

One of the inversion cases (variance of 4, 32 observation points, joint inversion of head and flux data) was chosen to investigate the effect of the truncation order (*P*) on the final inversion result. Inversions were performed using truncation orders of 25, 50, 100, 200, 400, 800, and 1600. The inversions were performed on a server with one Terabyte (1 Tb) memory, 4 processors (Intel Xeon CPU E7-4850 v4 @ 2.10 GHz) and 40 cores in parallel mode. Figure 8 shows the *Y*-field estimated for each *P* value, the effect on the correlation coefficient, and elapsed time for each geostatistical iteration. For a truncation order of 25, we capture an overly smooth version of the true model with a correlation coefficient of 0.84. By setting the truncation order to 50, 100, and 200, the correlation coefficient increases to 0.88, 0.91, and 0.94, respectively. The truncation order of 400 (used in our study) with a correlation coefficient of 0.96 is the point beyond which increasing the truncation order does not significantly improve the correlation coefficient. So, the truncation order leads to improvement of *Y*-field reconstruction up to some points and after this point, it is only the computational time that increases as the inversion performance is data limited. The computational time increased exponentially for large P values. The right choice of P is critical to ensure sufficient reconstruction of the hydraulic conductivity field while keeping the computational time low. The truncation order should be chosen based on the degree of heterogeneity and the computational resource available. It would help perform inversion using different numbers of principal components to ensure the proper choice of the number of principal components.

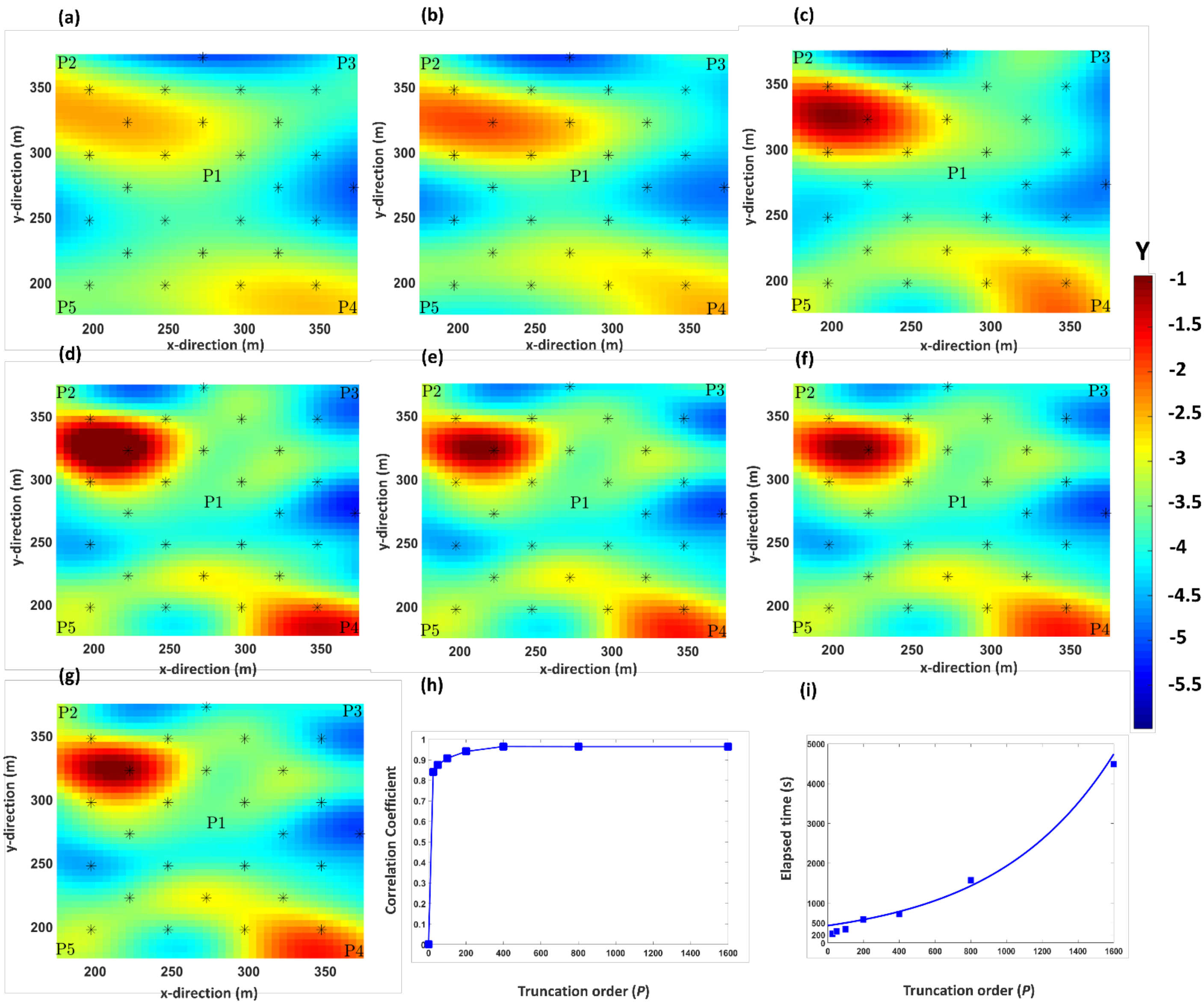

Figure 8: Estimated *Y*-field for truncation order of **(a)** 25, **(b)** 50, **(c)** 100, **(d)** 200, **(e)** 400, **(f)** 800, **(g)** 1600. **(h)** Correlation coefficient versus truncation order, **(i)** elapsed time per one iteration versus truncation order

5.4 Implications for field implementations

Our results highlight the added value of using the flux data individually or jointly with head data in hydraulic tomography to achieve an enhanced reconstruction of the hydraulic conductivity field compared to using head data alone. This improvement is particularly pronounced when considering a small number of observations, a more likely setting for field applications. However, using only flux data requires setting the borehole boundary condition to constant head, which is feasible (using pumps whose rates are controlled with water level) but would be more challenging than pumping at a constant rate during the field experiments. However, measuring the flux data during pumping (with constant rate) and joint inversion of both data would be quite feasible and removes the limitation of the borehole boundary condition. Moreover, if one could measure the head and flux data at the same location, by doubling the number of observations, the *Y*-field estimate would be significantly improved. The potential application of FO cables for pressure measurement is discussed by Bulter et al. (1999) and a recent application for drawdown measurements during pumping tests is demonstrated by Tiedeman and Barrash (2020).

The results presented in this paper are only valid for steady-state hydraulic tomography. Transient hydraulic tomography would probably result in better reconstruction of hydraulic conductivity field estimation and boundary conditions would probably not play a role anymore.

6. CONCLUSIONS

We used a numerical model representing a one-layer heterogeneous aquifer along with a geostatistical inversion approach (PCGA) to assess the information content of head and flux data. We varied the observation type, the number of observation points, the hydraulic conductivity variance (with the same field structure) and the borehole boundary conditions. For a small number of observation points, we find that flux data produced a better *Y*-field compared to head data. When increasing the number of observation points and using appropriate borehole boundary conditions, the effect of the data type vanishes, and all converge to the same results as the sampling distance between points becomes smaller. For the same number of observation points, if we are able to measure the head and flux data at the same location, joint inversion of head and flux data provides an improved estimate compared to the individual inversion of head or flux data due to the doubling of the number of observations. This means that the head and flux data measured at the same location provide complementary information. The type of borehole boundary conditions used in the tomography and modeling affects the inversion results. The appropriate boundary condition for head and flux data is constant rate and constant head, respectively, while joint inversion performance is independent of the boundary type. Inappropriate selection of borehole boundary conditions may result in an underestimation of the *Y*-field values. Measuring flux data during a hydraulic tomography experiment is now feasible, especially for shallow sandy aquifers where active Distributed Temperature Sensing, can be deployed using direct push method to install the fiber optic cables into the sediments. Since the inversion is particularly sensitive to the number of measurements, groundwater flux measurements by active DTS can be particularly useful since it may provide a large number of measurements thanks to the high spatial resolution of fiber optic temperature measurements. Moreover, it can be also particularly useful in aquifers where the head drop due to the pumping is small, but there may be high groundwater fluxes. This should lead to interesting developments of hydraulic tomography experiments in the near future.

7. ACKNOWLEDGMENTS

This work has received funding from the European 'Union's Horizon 2020 research and innovation program under the Marie Sklodowska - Curie grant agreement number 722028 (ENIGMA ITN). In our work we relied on the PCGA implementation in python (pyPCGA) by Lee et al. (2016) available on GitHub (https://github.com/jonghyunharrylee/pyPCGA/). We would like to appreciate SINTEF for providing free access to the Matlab Reservoir Simulator Tool (MRST) which is available on the SINTEF website (https://www.sintef.no/projectweb/mrst/).

CRediT authorship statement

Behzad Pouladi: Writing - original draft, Writing - review & editing, Methodology, Conceptualization, Software, Formal analysis, Investigation. **Niklas Linde**: Conceptualization, Methodology, Supervision, Writing, Supervision, Writing - original draft, Writing - review & editing. **Laurent Longuevergne**: Supervision. **Olivier Bour**: Writing - review & editing, Conceptualization, Writing - review & editing.

DECLARATION OF COMPETING INTEREST

The authors declare that they have no known competing financial interests or personal relationships that could have influenced the work reported in this paper.

REFERENCES

Alumbaugh, D.L., Newman, G.A., 2000. Image appraisal for 2-D and 3-D electromagnetic inversion. Geophysics 65, 1455–1467.

Bakker, M., Caljé, R., Schaars, F., van der Made, K., de Haas, S., 2015. An active heat tracer experiment to determine groundwater velocities using fiber optic cables installed with direct push equipment. Water Resour. Res. 51, 2760–2772.

Berg, S.J., Illman, W.A., 2015. Comparison of hydraulic tomography with traditional methods at a highly heterogeneous site. Groundwater 53, 71–89.

Berg, S.J., Illman, W.A., 2013. Field study of subsurface heterogeneity with steady- state hydraulic tomography. Groundwater 51, 29–40.

Berg, S.J., Illman, W.A., 2011. Three- dimensional transient hydraulic tomography in a highly heterogeneous glaciofluvial aquifer- aquitard system. Water Resour. Res. 47.

Bohling, G.C., Butler Jr, J.J., 2010. Inherent limitations of hydraulic tomography. Groundwater 48, 809–824.

Bohling, G.C., Butler Jr, J.J., Zhan, X., Knoll, M.D., 2007. A field assessment of the value of steady shape hydraulic tomography for characterization of aquifer heterogeneities. Water Resour. Res. 43.

Brauchler, R., Hu, R., Dietrich, P., Sauter, M., 2011. A field assessment of high- resolution aquifer characterization based on hydraulic travel time and hydraulic attenuation tomography. Water Resour. Res. 47.

Brauchler, R., Hu, R., Hu, L., Jiménez, S., Bayer, P., Dietrich, P., Ptak, T., 2013. Rapid field application of hydraulic tomography for resolving aquifer heterogeneity in unconsolidated sediments. Water Resour. Res. 49, 2013–2024.

Brauchler, R., Hu, R., Vogt, T., Al-Halbouni, D., Heinrichs, T., Ptak, T., Sauter, M., 2010. Cross-well slug interference tests: An effective characterization method for resolving aquifer heterogeneity. J. Hydrol. 384, 33–45.

Brauchler, R., Liedl, R., Dietrich, P., 2003. A travel time based hydraulic tomographic approach. Water Resour. Res. 39.

Butler Jr, J.J., McElwee, C.D., Bohling, G.C., 1999. Pumping tests in networks of multilevel sampling wells: Motivation and methodology. Water Resour. Res. 35, 3553–3560.

Cardiff, M., Bakhos, T., Kitanidis, P.K., Barrash, W., 2013. Aquifer heterogeneity characterization with oscillatory pumping: Sensitivity analysis and imaging potential. Water Resour. Res. 49, 5395–5410.

Cardiff, M., Barrash, W., 2011. 3-D transient hydraulic tomography in unconfined aquifers with fast drainage response groundwater flow parameters (primarily , hydraulic conductivity K) in permeable , unconfined aquifers . To invert the large amount of transient data collected from 3DT 47. https://doi.org/10.1029/2010WR010367

Cardiff, M., Barrash, W., Kitanidis, P.K., Malama, B., Revil, A., Straface, S., Rizzo, E., 2009. A potential- based inversion of unconfined steady- state hydraulic tomography. Groundwater 47, 259–270.

Day- Lewis, F.D., Singha, K., Binley, A.M., 2005. Applying petrophysical models to radar travel time and electrical resistivity tomograms: Resolution- dependent limitations. J. Geophys. Res. Solid Earth 110.

des Tombe, B.F., Bakker, M., Smits, F., Schaars, F., van der Made, K., 2019. Estimation of the variation in specific discharge over large depth using distributed temperature sensing (DTS) measurements of the heat pulse response. Water Resour. Res. 55, 811–826.

Doro, K.O., Cirpka, O.A., Leven, C., 2015. Tracer tomography: Design concepts and field experiments using heat as a tracer. Groundwater 53, 139–148.

Drost, W., Klotz, D., Koch, A., Moser, H., Neumaier, F., Rauert, W., 1968. Point dilution methods of investigating ground water flow by means of radioisotopes. Water Resour. Res. 4, 125–146.

Fakhreddine, S., Lee, J., Kitanidis, P.K., Fendorf, S., Rolle, M., 2016. Imaging geochemical heterogeneities using inverse reactive transport modeling: An example relevant for characterizing arsenic mobilization and distribution. Adv. Water Resour. 88, 186–197.

Fienen, M.N., Clemo, T., Kitanidis, P.K., 2008. An interactive Bayesian geostatistical inverse protocol for hydraulic tomography. Water Resour. Res. 44.

Fischer, P., Jardani, A., Soueid Ahmed, A., Abbas, M., Wang, X., Jourde, H., Lecoq, N., 2017. Application of Large- Scale Inversion Algorithms to Hydraulic Tomography in an Alluvial Aquifer. Groundwater 55, 208–218.

Gottlieb, J., Dietrich, P., 1995. Identification of the permeability distribution in soil by hydraulic tomography. Inverse Probl. 11, 353.

Huang, S., Wen, J., Yeh, T.J., Lu, W., Juan, H., Tseng, C., Lee, J., Chang, K., 2011. Robustness of joint interpretation of sequential pumping tests: Numerical and field experiments. Water Resour. Res. 47.

Illman, W. a, Liu, X., Craig, A., 2008. Evaluation of transient hydraulic tomography and common hydraulic characterization approaches through laboratory sandbox experiments. J. Environ. Eng. Manag. 18, 249–256.

Illman, W.A., Berg, S.J., Zhao, Z., 2015. Should hydraulic tomography data be interpreted using geostatistical inverse modeling? A laboratory sandbox investigation. Water Resour. Res. 51, 3219–3237.

Illman, W.A., Zhu, J., Craig, A.J., Yin, D., 2010. Comparison of aquifer characterization approaches through steady state groundwater model validation: A controlled laboratory sandbox study. Water Resour. Res. 46.

Jamin, P., Goderniaux, P., Bour, O., Le Borgne, T., Englert, A., Longuevergne, L., Brouyère, S., 2015. Contribution of the finite volume point dilution method for measurement of groundwater fluxes in a fractured aquifer. J. Contam. Hydrol. 182, 244–255.

Jim Yeh, T., 1992. Stochastic modelling of groundwater flow and solute transport in aquifers. Hydrol. Process. 6, 369–395.

Jiménez, S., 2015. High resolution aquifer characterization using hydraulic tomography and tracer tomography.

Jiménez, S., Mariethoz, G., Brauchler, R., Bayer, P., 2016. Smart pilot points using reversible-jump Markov- chain Monte Carlo. Water Resour. Res. 52, 3966–3983.

Kang, P.K., Lee, J., Fu, X., Lee, S., Kitanidis, P.K., Juanes, R., 2017. Improved characterization of heterogeneous permeability in saline aquifers from transient pressure data during freshwater injection. Water Resour. Res. 53, 4444–4458.

Klepikova, M. V, Le Borgne, T., Bour, O., de Dreuzy, J., 2013. Inverse modeling of flow tomography experiments in fractured media. Water Resour. Res. 49, 7255–7265.

Kowalsky, M.B., Finsterle, S., Rubin, Y., 2004. Estimating flow parameter distributions using ground-penetrating radar and hydrological measurements during transient flow in the vadose zone. Adv. Water Resour. 27, 583–599.

Kuhlman, K.L., Hinnell, A.C., Mishra, P.K., Yeh, T.J., 2008. Basin- scale transmissivity and storativity estimation using hydraulic tomography. Groundwater 46, 706–715.

Lee, J., Kitanidis, P.K., 2014. Large- scale hydraulic tomography and joint inversion of head and tracer data using the principal component geostatistical approach (PCGA). Water Resour. Res. 50, 5410–5427.

Lee, J., Kokkinaki, A., Kitanidis, P.K., 2018. Fast large-scale joint inversion for deep aquifer characterization using pressure and heat tracer measurements. Transp. Porous Media 123, 533–543.

Lee, J., Yoon, H., Kitanidis, P.K., Werth, C.J., Valocchi, A.J., 2016. Scalable subsurface inverse modeling of huge data sets with an application to tracer concentration breakthrough data from magnetic resonance imaging. Water Resour. Res. 52, 5213–5231.

Lie, K.-A., 2019. An introduction to reservoir simulation using MATLAB/GNU Octave: User guide for the MATLAB Reservoir Simulation Toolbox (MRST). Cambridge University

Press.

Liu, F., Yeh, T.J., Wang, Y., Hao, Y., Wen, J., Wang, W., 2020. Characterization of basin-scale aquifer heterogeneity using transient hydraulic tomography with aquifer responses induced by groundwater exploitation reduction. J. Hydrol. 588, 125137. https://doi.org/10.1016/j.jhydrol.2020.125137

Liu, S., Yeh, T.J., Gardiner, R., 2002. Effectiveness of hydraulic tomography: Sandbox experiments. Water Resour. Res. 38, 1–5.

Liu, X., Illman, W.A., Craig, A.J., Zhu, J., Yeh, T., 2007. Laboratory sandbox validation of transient hydraulic tomography. Water Resour. Res. 43.

Lochbühler, T., Doetsch, J., Brauchler, R., Linde, N., 2013. Structure-coupled joint inversion of geophysical and hydrological data. Geophysics 78, ID1–ID14.

Luo, N., Illman, W.A., Zha, Y., Park, Y.-J., Berg, S.J., 2020. Three-dimensional hydraulic tomography analysis of long-term municipal wellfield operations: Validation with synthetic flow and solute transport data. J. Hydrol. 125438.

Maldaner, C.H., Munn, J.D., Coleman, T.I., Molson, J.W., Parker, B.L., 2019. Groundwater flow quantification in fractured rock boreholes using active distributed temperature sensing under natural gradient conditions. Water Resour. Res. 55, 3285–3306.

Mao, D., Yeh, T.-C.J., Wan, L., Hsu, K.-C., Lee, C.-H., Wen, J.-C., 2013. Necessary conditions for inverse modeling of flow through variably saturated porous media. Adv. Water Resour. 52, 50–61.

Michael Tso, C., Zha, Y., Jim Yeh, T., Wen, J., 2016. The relative importance of head, flux, and prior information in hydraulic tomography analysis. Water Resour. Res. 52, 3–20.

Paradis, D., Gloaguen, E., Lefebvre, R., Giroux, B., 2015. Resolution analysis of tomographic slug test head data: Two- dimensional radial case. Water Resour. Res. 51, 2356–2376.

Paradis, D., Lefebvre, R., Gloaguen, E., Giroux, B., 2016. Comparison of slug and pumping tests for hydraulic tomography experiments: a practical perspective. Environ. Earth Sci. 75, 1159.

Read, T., Bour, O., Selker, J.S., Bense, V.F., Le Borgne, T., Hochreutener, R., Lavenant, N., 2014.

Active- distributed temperature sensing to continuously quantify vertical flow in boreholes. Water Resour. Res. 50, 3706–3713.

Revil, A., Karaoulis, M., Johnson, T., Kemna, A., 2012. Some low-frequency electrical methods for subsurface characterization and monitoring in hydrogeology. Hydrogeol. J. 20, 617–658.

Sayde, C., Thomas, C.K., Wagner, J., Selker, J., 2015. High- resolution wind speed measurements using actively heated fiber optics. Geophys. Res. Lett. 42, 10–64.

Schneider, H.A., Jackson, W.A., Rainwater, K., Reible, D., Morse, S., Hatzinger, P.B., Garza-Rubalcava, U., 2019. Estimation of Interstitial Velocity Using a Direct Drive High-Resolution Passive Profiler. Groundwater 57, 915–924.

Simon, N., Bour, O., Lavenant, N., Porel, G., Nauleau, B., Pouladi, B., Longuevergne, L., Crave, A., n.d. Numerical and experimental validation of the applicability of active- DTS experiments to estimate thermal conductivity and groundwater flux in porous media. Water Resour. Res. e2020WR028078.

Slater, L., 2007. Near surface electrical characterization of hydraulic conductivity: From petrophysical properties to aquifer geometries—A review. Surv. Geophys. 28, 169–197.

Somogyvári, M., Bayer, P., 2017. Field validation of thermal tracer tomography for reconstruction of aquifer heterogeneity. Water Resour. Res. 53, 5070–5084.

Soueid Ahmed, A., Jardani, A., Revil, A., Dupont, J.-P., 2016. Joint inversion of hydraulic head and self- potential data associated with harmonic pumping tests. Water Resour. Res. 52, 6769–6791.

Sun, R., Yeh, T.J., Mao, D., Jin, M., Lu, W., Hao, Y., 2013. A temporal sampling strategy for hydraulic tomography analysis. Water Resour. Res. 49, 3881–3896.

Tiedeman, C.R., Barrash, W., 2020. Hydraulic tomography: 3D hydraulic conductivity, fracture network, and connectivity in mudstone. Groundwater 58, 238–257.

Tosaka, H., Masumoto, K., Kojima, K., 1993. Hydropulse tomography for identifying 3-D permeability distribution, in: High Level Radioactive Waste Management: Proceedings. Volume 1.

Yeh, T.-C., Khaleel, R., Carroll, K.C., 2015. Flow through heterogeneous geologic media. Cambridge University Press.

Yeh, T.J., Liu, S., 2000. Hydraulic tomography: Development of a new aquifer test method. Water Resour. Res. 36, 2095–2105.

Yin, D., Illman, W.A., 2009. Hydraulic tomography using temporal moments of drawdown recovery data: A laboratory sandbox study. Water Resour. Res. 45.

Zha, Y., Yeh, T.-C.J., Mao, D., Yang, J., Lu, W., 2014a. Usefulness of flux measurements during hydraulic tomographic survey for mapping hydraulic conductivity distribution in a fractured medium. Adv. Water Resour. 71, 162–176.

Zha, Y., Yeh, T.J., Illman, W.A., Zeng, W., Zhang, Y., Sun, F., Shi, L., 2018. A reduced- order successive linear estimator for geostatistical inversion and its application in hydraulic tomography. Water Resour. Res. 54, 1616–1632.

Zha, Y., Yeh, T.J., Mao, D., Yang, J., Lu, W., 2014b. Advances in Water Resources Usefulness of flux measurements during hydraulic tomographic survey for mapping hydraulic conductivity distribution in a fractured medium. Adv. Water Resour. 71, 162–176. https://doi.org/10.1016/j.advwatres.2014.06.008

Zhao, Z., Illman, W.A., Berg, S.J., 2016. On the importance of geological data for hydraulic tomography analysis: Laboratory sandbox study. J. Hydrol. 542, 156–171.

Zhu, J., Yeh, T.-C.J., 2005. Characterization of aquifer heterogeneity using transient hydraulic tomography. Water Resour. Res. 41.

Declaration of interests

☒ The authors declare that they have no known competing financial interests or personal relationships that could have appeared to influence the work reported in this paper.

☐The authors declare the following financial interests/personal relationships which may be considered as potential competing interests:

CRediT authorship statement

Behzad Pouladi: Writing - original draft, Writing - review & editing, Methodology, Conceptualization, Software, Formal analysis, Investigation. **Niklas Linde**: Conceptualization, Methodology, Supervision, Writing, Supervision, Writing - original draft, Writing - review & editing. **Laurent Longuevergne**: Supervision. **Olivier Bour**: Writing - review & editing, Conceptualization, Writing - review & editing.